Nuclear Engineering and Technology 50 (2018) 297–305

Contents lists available at ScienceDirect

Nuclear Engineering and Technology

journal homepage: www.elsevier.com/locate/net

Original Article

Mechanical analysis of the bow deformation of a row of fuel assemblies in a PWR core

Andreas Wanninger [a], [*], Marcus Seidl [b], Rafael Macián-Juan [a]

[a] *Technical University of Munich, Department of Mechanical Engineering, Chair of Nuclear Technology, Boltzmannstr. 15, 85748 Garching, Germany*
[b] *PreussenElektra GmbH, Tresckowstr. 5, 30457 Hannover, Germany*

ARTICLE INFO

Article history:
Received 8 November 2017
Received in revised form
14 December 2017
Accepted 21 December 2017
Available online 12 January 2018

Keywords:
FEM Structural Model
Fuel Assembly Bow
PWR Fuel Assembly

ABSTRACT

Fuel assembly (FA) bow in pressurized water reactor (PWR) cores is considered to be a complex process with a large number of influencing mechanisms and several unknowns. Uncertainty and sensitivity analyses are a common way to assess the predictability of such complex phenomena. To perform such analyses, a structural model of a row of 15 FAs in the reactor core is implemented with the finite-element code ANSYS Mechanical APDL. The distribution of lateral hydraulic forces within the core row is estimated based on a two-dimensional Computational Fluid Dynamics model with porous media, assuming symmetric or asymmetric core inlet and outlet flow profiles. The influence of the creep rate on the bow amplitude is tested based on different creep models for guide tubes and fuel rods. Different FA initial states are considered: fresh FAs or FAs with higher burnup, which may be initially straight or exhibit an initial bow from previous cycles. The simulation results over one reactor cycle demonstrate that changes in the creep rate and the hydraulic conditions may have a considerable impact on the bow amplitudes and the bow patterns. A good knowledge of the specific creep behavior and the hydraulic conditions is therefore crucial for making reliable predictions.

1. Introduction

During thereactor operation, fuel assemblies (FAs) deform as a result of external forces and material parameter–related change mechanisms. This is of great practical importance because deformations may cause significant problems, such as grid damage or incomplete rod insertion events and may affect the power and flow distribution. The FAs deform most commonly in the first bending mode; that is, they exhibit a C-shaped bow, but bowing in higher bending modes is also observed, such as S-shaped and W-shaped bows. The latter are the least desirable because they present an increased risk for incomplete rod insertion and grid damage due to the decreased bending radius and the potentially higher number of interassembly contact points.

Since the occurrence of FA bow, operators and fuel vendors have tried to counteract the problem mainly by increasing the FA stiffness and creep resistance [1]. Because of these measures, FA deformations could be reduced in some instances but not completely eradicated because FA bow continues to be observed. At the same time, computational tools to predict the deformation of the fuel assemblies in the core have been developed to optimize the FA design and core planning. Still, owing to the complexity of the considered system, prediction uncertainties remain, regarding both the deformation amplitude and the direction. This may be associated with the high uncertainties about the boundary conditions, for example, the distribution of lateral hydraulic forces and the neutron flux–dependent material models. Within this project, we want to assess the modeling output uncertainty and parameter sensitivity of structural models representing this complex system. To perform such analyses, a reference fuel assembly structural model was developed in the finite-element code ANSYS Mechanical APDL to simulate the typical FA structural behavior [2]. As a first approach to understand the relative influence of many model parameters, a qualitative sensitivity analysis of the model was conducted in a previous work [3]. That analysis considered one single isolated FA and analyzed the sensitivity of the permanent FA deformation to different influencing parameters. For this purpose, a hypothetical discrete lateral force was applied at the mid-grid level over four reactor cycles. The outcome of that analysis showed that the uncertainties about the creep rate and the lateral hydraulic forces are at least as influential on the bow amplitude as possible changes to the FA structural stiffness (see Fig. 1). Furthermore, the influence of FA growth became more important for high burnup (BU).

---

* *Corresponding author.*
E-mail address: andreas.wanninger@ntech.mw.tum.de (A. Wanninger).

https://doi.org/10.1016/j.net.2017.12.009

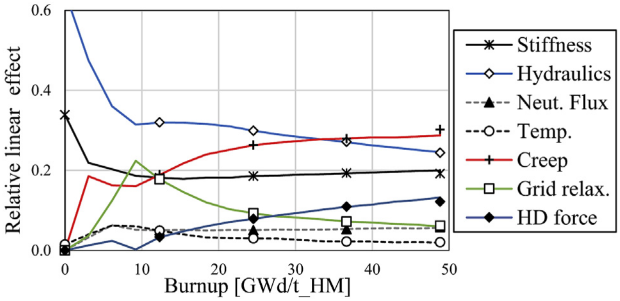

Fig. 1. Relative linear effects versus BU of different parameters [3].
BU, burnup; HD, holddown.

However, the shortcomings of that analysis are also clear. First, the fact of considering only a single FA does not account for the lateral constraints the FA is subjected to in the reactor. Next, only a discrete lateral force was applied instead of a realistic distribution of hydraulic forces. As for the creep models, only standard Zry-4 models were used without verifying their applicability to bending problems and more recent advanced materials. Moreover, lateral neutron flux and temperature gradients over the FA as they are present at the core periphery were not considered. For these reasons, in our study, we extended the analysis to a full 2-D model, considering the central row of 15 FAs in the reactor core. All new model features and assumptions are presented in the second section of this article. The third section discusses the simulation results. Considering the previous analysis, our emphasis lies on the influence of uncertainties about creep and lateral hydraulic forces. Finally, the effect of FAs with an initial bow from previous cycles is investigated.

2. Models and methods

2.1. FA row structural model

The FA structural model is based on the 16×16 design for KWU Vor-Konvoi plants. Fig. 2 gives a schematic representation of the model setup and its individual elements, which were described in [2,3]. The most important new feature of the structural model when an FA row is set up is that the neighboring FAs are coupled to each other at the grid levels with 1-D gap-contact elements. Contact between FAs is established if the relative displacement between two FAs is larger than the initial gap size $b_{\text{gap,ini}}$, thus coupling the FAs mechanically in the lateral translational degree of freedom (DOF). The initial gap size under operation is defined as $b_{\text{gap,ini}} = 1.6$ mm, which is the nominal value of the water gap between two FAs in hot condition [4]. For our analysis, we assumed this value to be constant for all interassembly gaps at all temperatures and BUs, ignoring grid growth, manufacturing tolerances, and other effects. Fig. 3 represents the undeformed system of 15 FAs. To better appreciate the FA deformations, the FAs are reduced to a curve defined by the displacements at grid levels 1–9 (top grid). The deformation of the FA row is limited by the presence of the left and right reactor walls at a distance of $b_{\text{gap,ini}}$ from FA 1 and 15.

Table 1 summarizes the FA boundary conditions used for the different simulation steps. Two in-core and one ex-core conditions are distinguished. During in-core operation, all DOFs at the FA head and foot are fixed, except for the axial and rotational displacement DOFs at the FA head, which result implicitly from the solution as a function of the holddown (HD) spring stiffness k_{HD}, the HD spring relaxation over BU, and the differential axial thermal expansion of the FAs and the core structures. At the beginning of cycle (BOC), an initial load step is simulated to set up the thermoelastic equilibrium under reactor operating conditions due the thermal and hydraulic loads, $T(x,z)$ and $\boldsymbol{f}_{\text{hyd}}(x,z)$, which are introduced in the following sections. After this initial step, the operation load step is started and includes creep and growth algorithms depending on the distribution of the fast neutron flux $\phi(x,z)$ and extends over 7,920 full-power hours until the end of cycle (EOC). In the cold condition, the temperature is decreased to 50°C, and the pumps are turned off, so that the hydraulic loads are withdrawn entirely. The mechanical constraints remain the same as during operation, but the HD force is increased due to the decreased temperature. The ex-core condition simulates isolated FAs lifted out of the open pressure vessel to obtain the unconstrained FA deformation, which is measurable during the outage. For this purpose, the FAs are decoupled by laterally drawing away the FAs from each other, thus opening all contact elements between them. Moreover, all rotational and HD constraints modeling the effect of the core plates are removed, thus creating a statically determinate system without external loading. Finally, an upward force about equal to the FA weight force W_{FA} is imposed on the top of the fuel assembly to account for the tensioning effect in the FA due to its weight when it is lifted.

2.2. Creep and growth laws

Because creep and—for high BU—growth proved to be very influential in the previous analysis, we undertook a more thorough analysis of guide tube (GT) creep and growth data. Two generations of zirconium alloys for GT materials are distinguished, Zircaloy-4 and advanced zirconium alloys with niobium content. No difference is made between the various types of advanced alloys by different vendors. This facilitates deriving correlations from experimental and performance data because a larger database is available. Because the fuel rods (FRs) are only coupled to the FA structure for low BU when the grid springs are not yet relaxed, FR creep and growth plays a minor role compared with that of GTs and is not treated explicitly in this article.

The measurement data underlying Yvon's Zry-4 GT creep law [5], which were used in the previous analysis, cover only a specific loading state, namely axial traction between 76 MPa and 94 MPa. Therefore, the validity of Yvon's creep law for other stress levels and loading patterns, particularly bending, needs to be confirmed. For this purpose, uniaxial creep measurement data for recrystallization-annealed Zry-4 from different authors [5,6,8,12] are compared with the predictions with Yvon's creep law (see the data and the corresponding curves in Fig. 4A). In general, we conclude that a good agreement of Yvon's creep response predictions exists with experimental data for traction, compression, and bending problems of recrystallization-annealed Zry-4 for a wide range of stresses from 7 MPa to 102 MPa and the temperatures of interest. In particular, we found a very good agreement with bending creep data by Pettersson [6]. Yvon's law has hence been proved adequate to model the creep response of Zry-4 GTs in the context of FA bow problems.

As for creep measurement data of advanced zirconium alloys, bending tests financed by SKI and the Swedish nuclear industry research co-operation (BFUK) were performed with two widely used GT materials in fresh and preirradiated conditions using the same setup as used for Pettersson's data. A best-estimate (BE) creep law with lower bounds and upper bounds (UB), Fig. 4B, was developed from the totality of data without regard to the preirradiation state because the preirradiation fluence was relatively low ($1 \times 10^{21}\text{ncm}^{-2}$). The observations in biaxial creep tests with the same materials suggest that the transient creep is practically saturated at the fluence of $1 \times 10^{20}\text{ncm}^{-2}$, at which the first data points were obtained in the bending creep tests. All data points are hence assumed to lie in the secondary creep regime, so that a

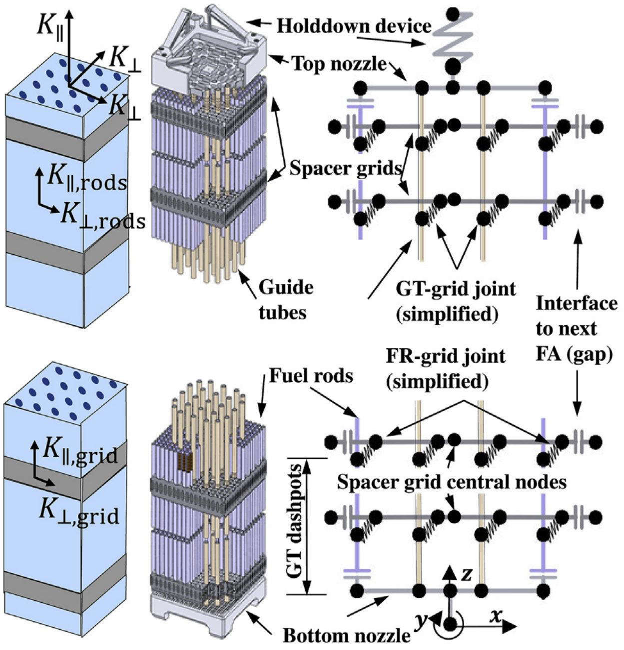

Fig. 2. As-fabricated FA and schematics of the FA structural model (right) and the FA porous hydraulic model (left). The depicted FA is different from the modeled FA design. FA, fuel assembly; FR, fuel rod; GT, guide tube.

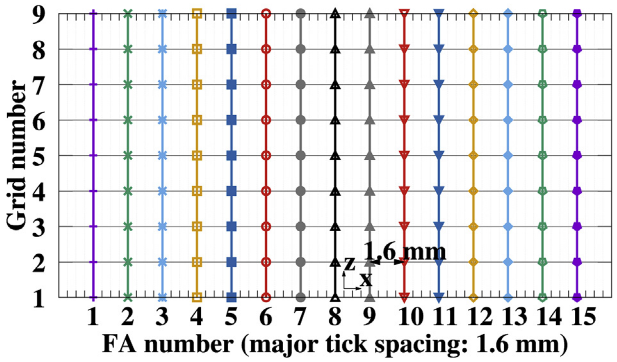

Fig. 3. Representation of the undeformed FA row.
FA, fuel assembly.

steady-state creep rate can be obtained by performing a linear regression. The intersection of the linear curve with the y-axis then represents the saturated primary creep strain. In this manner, a combined primary and secondary creep law, Equation (1), is obtained, summing up the influences of both contributions. The saturating fluence dependence of the primary creep is represented with a rational polynomial.

$$\varepsilon_{\mathrm{cr}} = \left(C_{\mathrm{cr,pri}} \frac{p_{\mathrm{cr}}\phi t}{1 + p_{\mathrm{cr}}\phi t} + C_{\mathrm{cr,sec}}\phi^{n_\phi} t \right) \sigma^{n_\sigma} e^{-Q_T/T} \tag{1}$$

The GT growth laws for Zry-4 and advanced alloys used in the structural model (see Fig. 5) are based on performance data [7]. Particularly for high BUs, usually large scattering of measurement data is observed depending on when breakaway growth with increased constant growth rates sets in. To test the influence of the increased growth rates on the structural model, a linear UB growth law is also implemented for the use with high-BU FAs. The value is obtained from measurements of accelerated growth of high-BU Zry-4 GT specimens with high hydrogen uptake [8]. For advanced alloys, a representative UB linear growth rate half that of Zircaloy-4 is assumed, which is in good agreement with the maximum of the performance data [7].

2.3. *FA row burnup model*

The local linear power density $q'(x,z)$, Equation (2), is defined by the core-averaged linear power density q'_{ave} multiplied by a radial factor $a_r(x)$ and an axial factor $a_z(z)$. Instead of a continuous distribution, the radial factor is the sum of two components:

- The averaged radial power factor of the respective fuel assembly $a_{r,i}$ defined by its position i in the FA row.
- The averaged and linearized lateral power gradient $g_{\mathrm{lat},i}$ over each fuel assembly. The resultant radial factor is then a function of the local cross-sectional coordinate x_i of the considered FA with the origin in the FA central axis.

Figs. 6A and 6B represent graphically the lateral and axial profiles. The fast neutron flux ($E_{\mathrm{n}} > 1\mathrm{MeV}$) $\phi(x,z)$, which is the basis for the calculation of the irradiation creep, relaxation, and growth processes, is then linearly linked to $q'(x,z)$ by a typical conversion factor c (see Equation (3)). For the FA structure, the temperature $T(z)$ is assumed to be equal to that of the surrounding coolant and is linearly interpolated between the core inlet and outlet temperatures from the bottom to the top of the active region. The FR cladding temperatures $T(x,z)$ are derived as a function of $q'(x,z)$ from heat transfer coefficients [9] between the coolant and cladding. Fig. 6C gives the corresponding temperature distribution in GTs (inner tubes) and FRs for averaged core power conditions. For the time being, we consider no evolution of the power density due to BU effects or due to changes in the interassembly water gaps. Over the FA row, a heterogeneous BU configuration is implemented according to a typical loading pattern in the central core row. For this purpose, three different FA burnup conditions are defined for the simulation runs: Fresh (F), medium BU (M), and high BU (H). Table 2 gives the initial conditions for the different cases with regard to effective growth, including the effect of HD spring relaxation and the grid spring relaxation (see also Ref. [2,3] for details). For the high-BU FAs, additionally a case with UB growth is considered. The BU condition used at the respective position is marked in Fig. 6A.

$$q'(x,z) = a_r(x)a_z(z)q'_{\mathrm{ave}} \text{ with } a_r(x) = a_{r,i} + g_{\mathrm{lat},i}x_i \tag{2}$$

$$\phi(x,z) = cq'(x,z) \tag{3}$$

2.4. *FA row hydraulic model*

The lateral hydraulic forces due to cross flow appear to be one of the main drivers of the FA bow and were very influential in the previous screening sensitivity analysis. For a more realistic estimation of the lateral hydraulic forces, numerical Computational Fluid Dynamics (CFD) calculations were necessary. Within our framework, the objective was not to predict the lateral hydraulic forces as accurately as possible, but to investigate the relative effect of parameter changes. Therefore, it was not necessary to create a detailed CFD model with resolved structures, but it was sufficient to design an approximate 2-D porous-medium model, representing the central core plane in which the FA row was positioned. With this approach, distributed momentum sinks S_{M} induce the pressure gradient due to the frictional and form drag effect of the structures (see Equations (4) and (5)), where $K_\parallel$ and $K_\perp$ are the pressure loss

Table 1
FA boundary conditions for different simulation steps.

Condition	Constraints						Loads		
	FA foot			FA head			Thermal	Neutron flux	Hydraulic
	u_x	u_z	θ_y	u_x	u_z	θ_y			
In-core under operation	0	0	0	0	$f(k_{\mathrm{HD}}, T, BU)$		$T(x,z)$	$\phi(x,z)$	$\boldsymbol{f}_{\mathrm{hyd}}(x,z)$
In-core in cold condition (CC)	0	0	0	0	$f(k_{\mathrm{HD}}, T, BU)$		50°C	0	0
Ex-core and lifted FAs	0	0	—	0	W_{FA}	—	50°C	0	0

BU, burnup; FA, fuel assembly; HD, holddown.

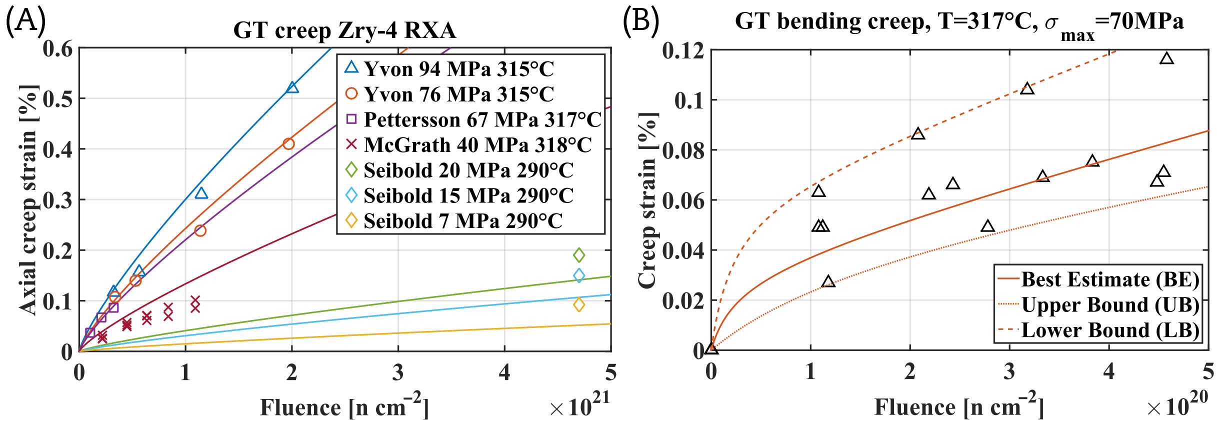

Fig. 4. Comparison of GT creep measurement data and used creep model.**(A)** Comparison for RXA Zry-4.**(B)** Comparison for advanced Zirconium alloys.
GT, guide tube; RXA, recrystallization-annealed.

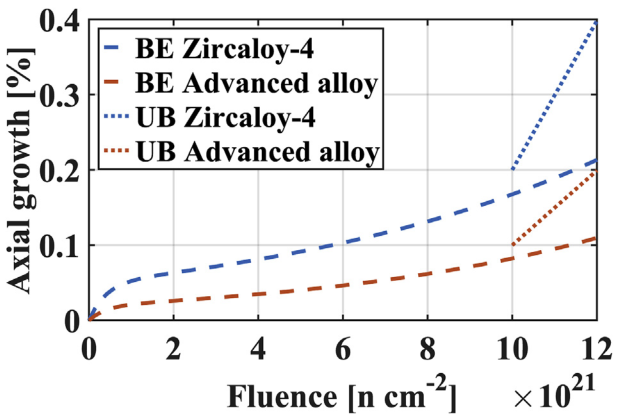

Fig. 5. Representation of GT growth laws.
BE, best-estimate; GT, guide tube; UB, upper-bound.

coefficients parallel and transverse to the structure. For the proposed model, the axial and transverse loss coefficients for both rod bundle and spacer grid regions need to be determined: $K_{\parallel,\mathrm{rods}}$, $K_{\parallel,\mathrm{grid}}$, $K_{\perp,\mathrm{rods}}$, and $K_{\perp,\mathrm{grid}}$ which are represented schematically in Fig. 2. No hydraulic resistance is assumed in the gaps, that is, $K_{\parallel,\mathrm{gap}} = K_{\perp,\mathrm{gap}} = 0$. The axial loss coefficients $K_{\parallel}$ for the grid and rod regions are defined based on validated thermohydraulic correlations [9,10]. The definition of the lateral loss coefficients is more challenging. Cross flow inside nuclear reactors has an important axial component due to the high mass flow rate through the core. The flow corresponds to an oblique flow over a rod bundle with a small angle of attack $\theta \ll 90^{\circ}$. With decreasing values of θ, the contribution of pressure drag to the flow resistance decreases in favor of friction drag, thus reducing the flow resistance. To obtain the pressure drop of the oblique flow, a resistance reduction ratio $\psi(\theta)$ is applied to the flow resistance coefficient obtained from pure cross flow $K_{\perp,90^{\circ}}$ [10]. The correlation obtained with the EOLE test section [11], Equation (6), is one of the few correlations for $\psi(\theta)$ in the literature which was specifically developed for PWR rod bundles. The EOLE correlation was additionally validated with experimental tests inside a water flow loop with an FA mock-up and the possibility to inject cross flow, the MISTRAL test section. To validate the EOLE correlation for use in our porous model, the experiments in the MISTRAL test section are simulated with a dedicated model in ANSYS CFX. Fig. 7A compares the experimental results for the lateral hydraulic force on the FA mock-up obtained with the MISTRAL test section with the CFX results. The EOLE correlation provides simulation results which are in very good agreement with the experiment and can be judged sufficiently reliable to provide a good estimation of the lateral pressure drop in PWR cross flow within our project. As for the definition of $K_{\perp,\mathrm{grid}}$, we assume that the grid redirects the flow completely into the axial direction after entering into the grid region with an arbitrary angle of attack θ. The lateral loss coefficient for the grid $K_{\perp,\mathrm{grid}}$ can hence be estimated based on the lateral reaction force on the grid due to the direction change.

$$S_{\mathrm{M},\parallel} = -K_{\parallel}\frac{\rho}{2}|\boldsymbol{v}|v_{\parallel} \tag{4}$$

$$S_{\mathrm{M},\perp} = -K_{\perp}\frac{\rho}{2}|\boldsymbol{v}|v_{\perp} \tag{5}$$

$$K_{\perp}(\theta) = \psi(\theta)K_{\perp,90^{\circ}} = \left(\sin\theta/\cos\left(\frac{90^{\circ}-\theta}{2}\right)\right)^{1.7}K_{\perp,90^{\circ}} \tag{6}$$

Fig. 7B shows the meshed domain implemented in ANSYS CFX, representing the entire row of 15 FAs. The mesh is refined in the

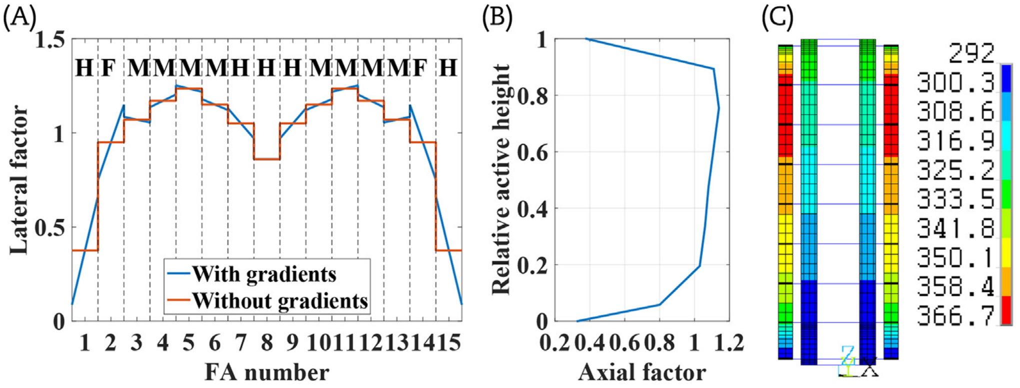

Fig. 6. Lateral and axial power profiles and derived temperature distribution. **(A)** Lateral power and BU profile. **(B)** Axial power profile. **(C)** Temperature [°C] distribution for average power.
FA, fuel assembly.

Table 2
Initial parameters for different BU conditions.

Case	BU	Effective growth[a]			Grid relaxation[b]		
	[GWd/t_{HM}]	law	Zry-4	Advanced alloy	Zr-alloy	Inconel	Evolution
Fresh (F)	0	BE	0 mm	0 mm	0%	0%	Decreasing
Medium (M)	15–40	BE	0 mm	0 mm	99%	25%	Constant
High (H)	>40	BE	5 mm	2.5 mm	99%	25%	Constant
High (H)	>40	UB	10 mm	5 mm	99%	25%	Constant

BE, best-estimate; BU, burnup; UB, upper-bound.
[a] Estimated average values based on the FA growth performance data in Ref. [7].
[b] Assumed values based on the considerations in Ref. [2].

grid and gap regions. A two-way fluid-structure interaction can be established by updating over time the position and size of the gaps in the modeled domain according to the FA structural deformation. The flow redistribution inside the core due to nonuniform core velocity inlet and outlet profiles is likely to be one of the drivers of FA bow. Based on specific observations made in experimental tests and numerical simulations given in the literature, we define hypothetical symmetric inlet and outlet flow profiles (see Fig. 7C). However, often asymmetric bow patterns have been observed, which cannot be explained by symmetric flow in the core. An asymmetric condition is necessary to obtain such deformations. Accordingly, an additional asymmetric velocity inlet profile is assumed. It is based on the symmetric profile, but the maximum is shifted a distance of two FA pitches to the left. Using these profiles as boundary conditions, the code evaluates the redistribution of the flow inside the core plane as a result of the pressure gradients originating from the nonhomogeneous flow distribution.

The lateral hydraulic force on the FA structure in a certain rod or grid region is obtained by integrating over the body force due to the porous medium in this region given by the CFD model solution. The resulting distribution serves as the data source for the lateral hydraulic loads in the structural model. Fig. 8 shows the distribution of line forces over each FA averaged over each grid and rod region for both symmetric and shifted inlet flow profiles. The line forces are clearly higher in the grid regions due to the increased flow resistance. For the case with symmetric inlet and outlet profile (Fig. 8A), the forces are maximum close to the FA extremities. In the core center, the influence of the boundaries nearly vanishes. That is, the flow redistribution is limited to the first and last third of the core. For the case with asymmetric inlet and symmetric outlet profile (Fig. 8B), the symmetry is clearly broken. The forces in the center of the core are significantly higher because the amount of flow to be redistributed increased due to the asymmetry. There is hence a twofold detrimental effect on the FA structure. Not only do the total lateral forces increase but also the effect on the FA structure is increased more than linearly due to the redistribution of forces towards the axial center. Only a negligible feedback of the FA deformation on the hydraulic forces was observed for the cases discussed in this article. Therefore, the hydraulic forces are considered constant over time.

3. Results

3.1. Symmetric hydraulic conditions

In this first simulation, the symmetric lateral hydraulic load distribution given in Fig. 8A was applied. Owing to the symmetry, we could use this case to estimate the beneficial effect when using FAs with advanced alloys. For this purpose, the FAs to the left (1–7) are assumed to be made of conventional Zry-4, whereas the FAs to the right (8–15) are made of advanced alloys. Fig. 9 gives the FA deformations for different times (BOC or EOC) and conditions according to Table 1. Fig. 9A depicts the thermoelastic equilibrium in the FA row at BOC under operation. Whereas the medium-BU and high-BU FAs are clearly deformed in the direction of the hydraulic force, the fresh FAs exhibit only little deformation, which is due to the higher stiffness and due to the inward bending as a result of the differential elongation of the FRs due to the thermal gradient. As operation advances, the FAs deform slowly toward the core shroud due to creep. At EOC under operation (Fig. 9B), only four FAs in the center remain without contact. After transition to cold condition and turning off the pumps (Fig. 9C), the overall deformation is reduced because the elastic component is removed. It becomes evident that toward the end of cycle, the lateral hydraulic forces on FAs 1–5 were mostly absorbed by the core shroud because their deflection amplitude only decreases slightly. As for the ex-core deformation of the FAs (Fig. 9D),

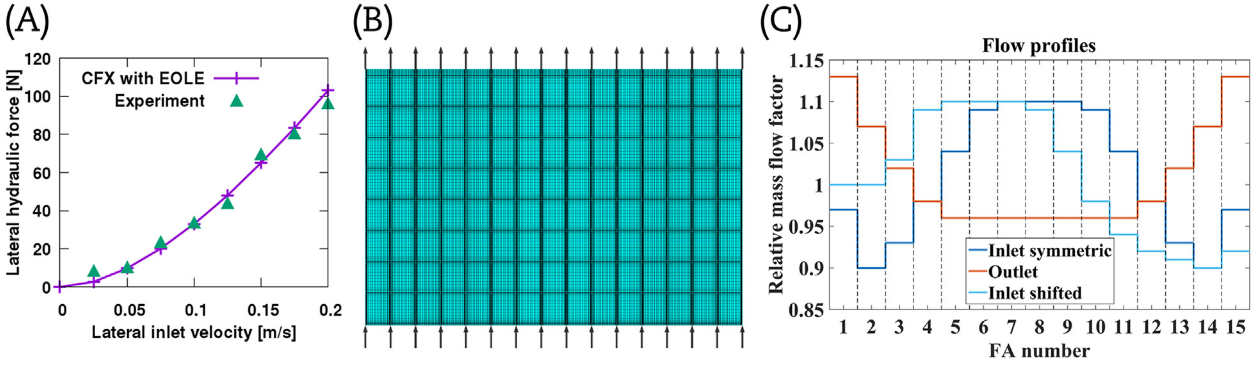

Fig. 7. FA hydraulic model. **(A)** Results for validation simulation. **(B)** Meshed domain (not to scale). **(C)** Inlet and outlet profiles. FA, fuel assembly.

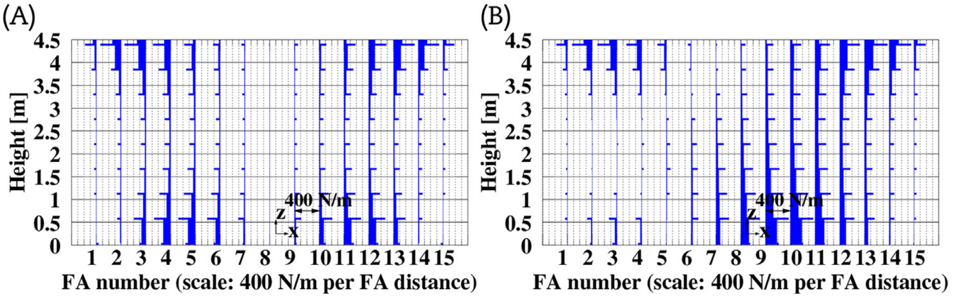

Fig. 8. Region-averaged lateral hydraulic line forces. **(A)** For symmetric inlet and outlet profile. **(B)** For asymmetric inlet and symmetric outlet profile. FA, fuel assembly.

the amplitude is decreased clearly due to the stress stiffening effect when the FAs are lifted. The Zry-4 FA 6 undergoes the largest deformation of nearly 6 mm. For the advanced-alloy FAs, the maximum deflection is reduced by nearly 25% compared with Zry4, which underlines the importance of the creep rate for the bow problem.

3.2. *Asymmetric hydraulic conditions*

From this point, only FAs with advanced-alloy GT and FR materials are investigated because they have become the standard in most Western PWRs. As the first approach to an uncertainty analysis, we wanted to investigate the effect of possible changes to the hydraulic, creep, and growth parameters on the outcome of the solution. In the first step, only the hydraulic condition is changed, switching from the symmetric inlet profile to the asymmetric inlet profile in the hydraulic model. Because of the asymmetric force distribution (Fig. 8B), the maxima for the elastic deflection occur for the FAs at the right (see Fig. 10A). Owing to the unilateral force on most FAs, they deform mostly in the first bending mode and exhibit C shapes. Only FA 5 undergoes forces in opposite directions at the bottom and the top and deforms in the second bending mode, resulting in an S shape. Considering the final ex-core bow shapes (Fig. 10B), FAs 2–8 exhibit strongly different shapes compared with the result with symmetric hydraulic conditions (Fig. 9D at the right). For FAs 9–15, an increase in bow amplitudes is observed with the total maximum increasing from 4.52 mm to 5.83 mm. The second step investigates two extremal cases within the uncertainty bounds of the established creep and growth models. For this purpose, we sought to create one simulation with maximum positive (+) amplitudes and one with maximum negative (−) amplitudes, only by modifying the creep and growth rates within the uncertainty bounds and without changing the hydraulic condition.

Table 3 summarizes the creep and growth conditions assumed for the different FAs to generate the different bow patterns. Figs. 10C and 10D give the ex-core results for the two extremal cases, whereas Fig. 10B represents the BE result. Between the (−) case and the (+) case, there are important differences regarding both the FA deformation amplitude and pattern. The maximum amplitude is increased by more than 50% solely due to the uncertainty about the creep law. As for the deformation pattern, a particularly strong effect becomes evident for the peripheral FAs undergoing UB growth. The inward bow due to the accelerated differential growth significantly outweighs bow due to the creep as a result of the outward hydraulic forces. The deformation amplitude and shape of the concerned FAs change strongly compared with those of the BE case. As for the high-BU FAs placed at positions with high flux gradients, there is hence a high uncertainty about the final deformation pattern.

3.3. *FAs with initial bow*

So far, the analyses have only included straight FAs at BOC, no matter the assumed BU level. In reality, FAs with nonzero BU may exhibit initial bow from previous cycles, thus perturbing the initially straight system. To investigate the effect of such FAs on the system, three different FAs with initial bow are introduced into the FA row: one FA with an S shape at position 3, one FA with a C shape and high deformation at position 11, and one FA with a C shape and reduced deformation at position 14. The deformations of these three FAs are generated in the first reactor cycle. Fig. 11A gives their ex-core bow shapes at EOC 1. Then the prebowed FAs are constrained and coupled to the other straight FAs in the second cycle of the same run (see Fig. 11B for the resulting equilibrium in cold condition). Starting from this state, two different simulations are

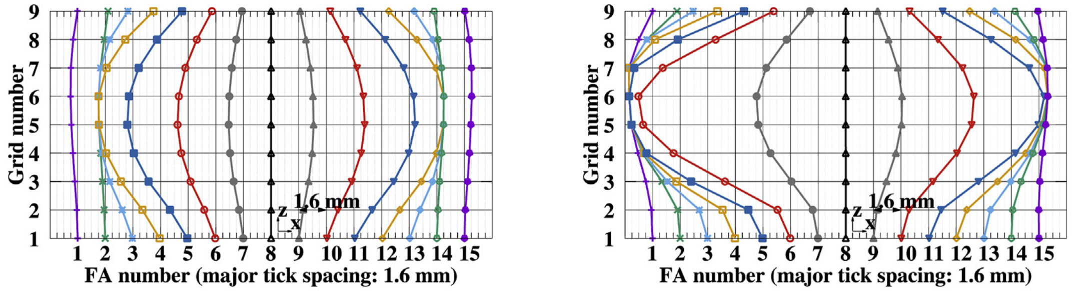

(A)BOC, Operation, $u_{x,\max,\mathrm{Zry}}$=3.59 mm, $u_{x,\max,\mathrm{adv}}$=3.59 mm (C) EOC, CC, $u_{x,\max,\mathrm{Zry}}$=8.82 mm, $u_{x,\max,\mathrm{adv}}$=6.70 mm

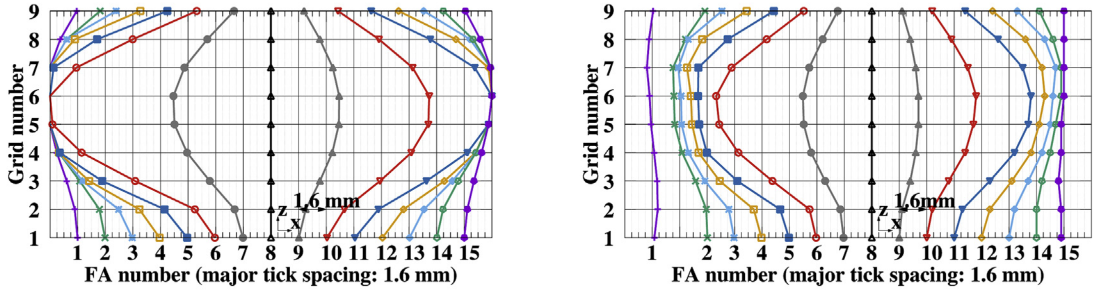

(B) EOC, Operation, $u_{x,\max,\mathrm{Zry}}$=9.60 mm,$u_{x,\max,\mathrm{adv}}$=8.00 mm (D)EOC, Ex-core, $u_{x,\max,\mathrm{Zry}}$=5.87 mm, $u_{x,\max,\mathrm{adv}}$=4.52 mm

Fig. 9. FA deformation in different phases using the symmetric hydraulic conditions.
BOC, beginning of cycle; CC, cold condition; EOC, end of cycle; FA, fuel assembly.

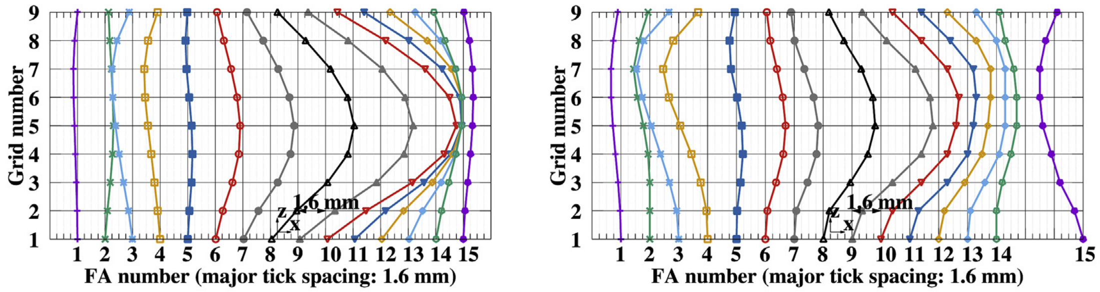

(A)BOC, Operation, $u_{x,\max}$=7.61 mm, $u_{x,\mathrm{RMS}}$=2.89 mm (C) (−) EOC, Ex-core, $u_{x,\max}$=4.41 mm, $u_{x,\mathrm{RMS}}$=1.87 mm

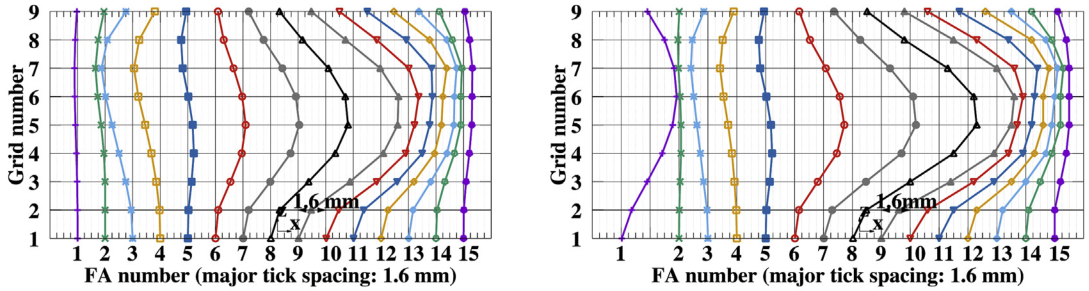

(B) BE, EOC, Ex-core, $u_{x,\max}$=5.83 mm, $u_{x,\mathrm{RMS}}$=2.36 mm (D) (+), EOC, Ex-core, $u_{x,\max}$=7.31 mm, $u_{x,\mathrm{RMS}}$=2.51 mm

Fig. 10. FA deformations for different creep and growth uncertainty assumptions using the asymmetric hydraulic conditions.
BE, best-estimate; BOC, beginning of cycle; EOC, end of cycle; FA, fuel assembly.

performed. Fig. 11C gives the results of the first simulation, performed without lateral hydraulic forces and gradients over the FAs to assess the isolated effect of the initial bow. Owing to the mechanical coupling between the FAs, the deflection amplitude of the FAs with initial bow is reduced, up to nearly one half for FA 11. On the other hand, the FAs neighboring the prebowed assemblies remain permanently deformed due to the interaction. The second simulation is performed with the symmetric hydraulic forces used in Section 3.1 to appreciate the perturbing effect of the initial bow on the final result in Fig. 11D compared with that of FAs 9–16 in Fig. 9D. Owing to the effect of the unilateral hydraulic forces, the S shape of FA 3 is transformed into an inversed P shape, which represents a superposition of the first and second bending modes. For FA 11, the formation of a W shape is observed while its amplitude is

Table 3
Creep and growth models used for the extremal cases: lower-bound (LB), best-estimate (BE), or upper-bound (UB).

Case	FA #:	1	2	3	4	5	6	7	8	9	10	11	12	13	14	15
(−)	Growth	BE						UB	BE							UB
	Creep	UB				BE	LB									
(+)	Growth	UB	BE							UB	BE					
	Creep	LB				BE	UB									

reduced to less than a quarter of the original value. For FA 14, the bow direction is the inverse due to the creep deformation due to the hydraulic loads, resulting in a P-shaped bow. As for the initially straight FAs, a clear difference in the bow pattern can be observed compared with the deformation of the reference state with only straight FAs at BOC in Fig. 9D. This confirms the strong effect of the initial bow on the final bow patterns.

4. Discussion

This article described simulations of the creep deformation of the FA structure in a single FA row in a PWR core. We investigated the influence of both modeling uncertainties and bow before the irradiation cycle on the final bow shapes after one cycle of operation. The resulting bow shapes were in good agreement with what was observed in ex-core bow measurements of PWR FAs: C shapes were the most common, but also P, S, and W shapes were detected. First, the reference simulation with a symmetric hydraulic force distribution was performed, and the sensitivity of the solution to the creep resistance of different materials was demonstrated. Then, the role of the uncertainties in the model was investigated. The simulations confirmed the tendencies obtained from a previous screening sensitivity analysis: both the hydraulic condition in the core and the uncertainty about the creep rates have an equally important impact on the final bow pattern. The specific creep law affects mostly the deformation rate, whereas changes in the hydraulic condition may fundamentally modify the bow pattern. Given the limited knowledge about the boundary conditions inside an operating core and their time behavior, it was a challenge to predict a specific unique bow pattern. Instead, we determined the distribution of potential bow patterns. To characterize the spread of the model predictions, several statistical measures exist, which will

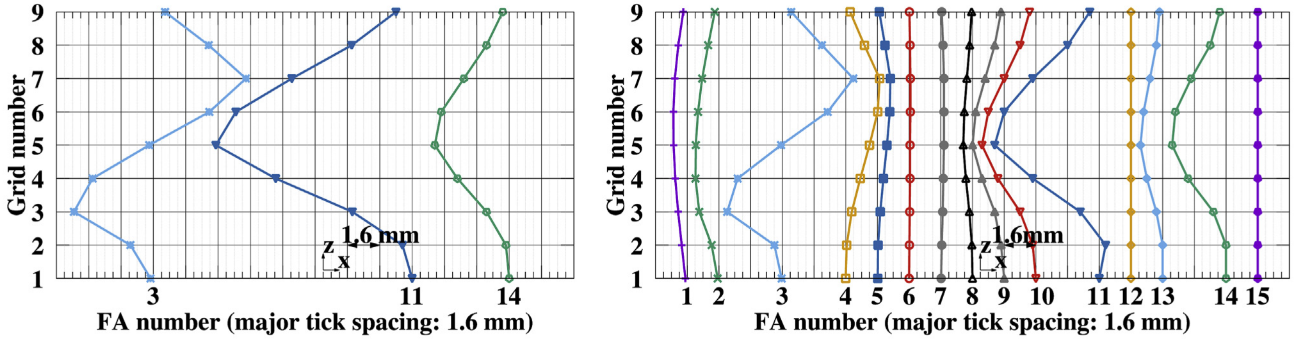

(A) EOC 1, Ex-core, $u_{x,\max}$=9.71 mm, $u_{x,\mathrm{RMS}}$=1.88 mm (C) EOC 2, Ex-core, $u_{x,\max}$=5.20 mm, $u_{x,\mathrm{RMS}}$=1.32 mm

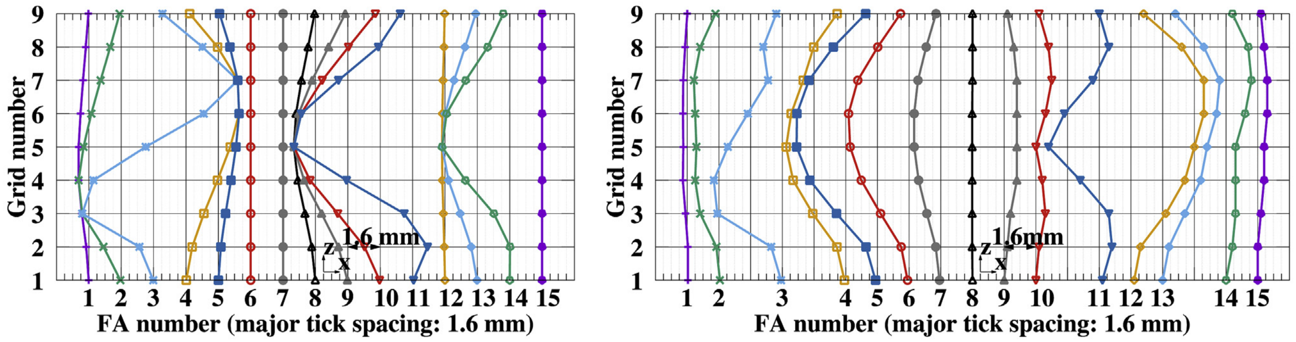

(B) BOC 2, CC, $u_{x,\max}$=5.87 mm, $u_{x,\mathrm{RMS}}$=1.74 mm (D) EOC 2, Ex-core, $u_{x,\max}$=4.08 mm, $u_{x,\mathrm{RMS}}$=1.67 mm

Fig. 11. FA deformations when introducing FAs with initial bow.
BOC, beginning of cycle; EOC, end of cycle; FA, fuel assembly.

be evaluated in a future step. Finally, simulation runs over two reactor cycles were presented, in which only certain FAs were deformed in the first cycle and then coupled to the other straight FAs in the second cycle of the same run. This illustrated how bow patterns can propagate over several cycles. It indicated, furthermore, that if the bow shapes are not measured after each cycle, the initial bow imposes another source of uncertainty on the predictions. In practice, this means that it is necessary to implement a transfer of the final stress and strain states of bowed FAs after one irradiation cycle as an initial condition to a new run. In addition, grid growth must be accounted for by modifying the initial gap size of the contact elements as a function of fluence and temperature. In this manner, the propagation of bow patterns can be simulated flexibly for any FA reshuffling plan.

For further studies, our specific interest lies in extending the simulations to the full-core system. The FA structural model presented in this article was designed as a full 3-D model and, therefore, takes into account that the deformations in the cross-sectional directions are not independent of each other. For example, the evolution of the creep rate is often nonlinear in the strain or stress dependence, leading to different creep rates if two load states are superposed. Moreover, loading the FA simultaneously in both cross-sectional directions modifies the FA lateral stiffness due to the characteristics of the frictional FR support: rotationally loading the grid-to-rod connection about one axis affects the frictional behavior in the perpendicular direction. Common 2-D–only FA structural models ignore these nonlinearities and separately calculate the deformation of each FA row in each lateral direction of the reactor core, although a full 3-D structural model might be indispensable to duly account for these effects. In addition, a coupling of the mechanical model to neutronics calculations can be considered in the future to account for the feedback of power density changes on the bow deformation. However, for such a coupled 3-D system, it can be expected that the variance of the bow patterns will further increase due to the higher number of DOFs. Moreover, it also implies a strong increase in computational expense and will require new solutions to enhance performance.

In conclusion, our results demonstrated the important challenges in FA bow modeling and suggest that bow calculations should be accompanied by an uncertainty analysis to estimate the variability of the model predictions. Provided that the uncertainties are accounted for, future FA bow prediction models can offer important support to operators about the expected bow patterns for a specific core loading plan.

Conflict of interest

The authors have no conflicts of interest to declare.

Acknowledgments

The main author would like to acknowledge PreussenElektra GmbH for their financial support and Vattenfall for kindly providing data on guide tube creep.

References

[1] G. Gentet, C. Hintergräber, P. Louf, N. Teboul C. Wiltz, Areva product experience in support of EPR fuel design, In: TopFuel 2012 Transactions, Manchester, UK, September 2–6, 2012.
[2] A. Wanninger, M. Seidl R. Macián-Juan, Development of computational methods to describe the mechanical behavior of PWR fuel assemblies, In: Proceedings of the 47th Annual Meeting on Nuclear Technology (AMNT 2016), Hamburg, Germany, May 10–12, 2016.
[3] A. Wanninger, M. Seidl R. Macián-Juan, Screening sensitivity analysis of a PWR fuel assembly FEM structural model, In: TopFuel 2016 Conference Proceedings, Boise, USA, September 11–16, 2016.
[4] RSK, Verformungen von Brennelementen in deutschen Druckwasserreaktoren (DWR), RSK-Stellungnahme (474. Sitzung der Reaktor-Sicherheitskommission (RSK) am 18.03.2015), 2015 [In German].
[5] P. Yvon, J. Diz N. Ligneau, Irradiation creep and growth of guide Thimble alloys, In: Proceedings of the International Symposium Fontevraud IV, Paris, France, September 14–18, 1998.
[6] K. Pettersson, Evaluation of Results from an In-pile Creep Test in the Studsvik R2 Reactor, SKI, Report 02:48, Stockholm, Sweden, 2002.
[7] G. Wikmark, L. Hallstadius, K. Yueh, Cladding to sustain corrosion, creep and growth at high burn-ups, Nuclear Eng. Technol. 41 (2009) 143–148.
[8] M.A. McGrath, S. Yagnik, Experimental investigation of irradiation creep and growth of recrystallized Zircaloy-4 guide tubes pre-irradiated in PWR, J. ASTM Int. 8 (2011) 875–898.
[9] N.E. Todreas, M.S. Kazimi, Nuclear Systems, second ed., vol. 1, CRC Press, Boca Raton, USA, 2012.
[10] I.E. Idelchik, Handbook of Hydraulic Resistance, third ed., CRC Press, Boca Raton, USA, 1994.
[11] J. Peybernès, Evaluation of the forces generated by cross-flow on PWR fuel assembly, in: IAEA-TECDOC-1454 Structural Behaviour of Fuel Assemblies for Water Cooled Reactors, Vienna, Austria, 2005.
[12] A. Seibold, F. Garzarolli R. Manzel, Material development for Siemens fuel elements, In: International Topical Meeting on Light Water Reactor Fuel Performance, Park City, USA, April 10–13, 2000.